

Thermodynamic Considerations for Thermal Water Splitting Processes and High Temperature Electrolysis

IMECE 2008

J. E. O'Brien

November 2008

The INL is a
U.S. Department of Energy
National Laboratory
operated by
Battelle Energy Alliance



This is a preprint of a paper intended for publication in a journal or proceedings. Since changes may be made before publication, this preprint should not be cited or reproduced without permission of the author. This document was prepared as an account of work sponsored by an agency of the United States Government. Neither the United States Government nor any agency thereof, or any of their employees, makes any warranty, expressed or implied, or assumes any legal liability or responsibility for any third party's use, or the results of such use, of any information, apparatus, product or process disclosed in this report, or represents that its use by such third party would not infringe privately owned rights. The views expressed in this paper are not necessarily those of the United States Government or the sponsoring agency.

IMECE2008 - 68880

THERMODYNAMIC CONSIDERATIONS FOR THERMAL WATER SPLITTING PROCESSES AND HIGH TEMPERATURE ELECTROLYSIS

J. E. O'Brien

Idaho National Laboratory
Idaho Falls, ID 83415, USA

ABSTRACT

A general thermodynamic analysis of hydrogen production based on thermal water splitting processes is presented. Results of the analysis show that the overall efficiency of any thermal water splitting process operating between two temperature limits is proportional to the Carnot efficiency. Implications of thermodynamic efficiency limits and the impacts of loss mechanisms and operating conditions are discussed as they pertain specifically to hydrogen production based on high-temperature electrolysis. Overall system performance predictions are also presented for high-temperature electrolysis plants powered by three different advanced nuclear reactor types, over their respective operating temperature ranges.

INTRODUCTION

There is a growing interest in the development of large-scale non-fossil hydrogen production technologies. This interest is driven by the immediate demand for hydrogen for refining of increasingly low-quality petroleum resources (e.g., the Athabasca oil sands, coal) [1, 2], the expected intermediate-term demand for carbon-neutral synthetic fuels [3], and the possible long-term demand for carbon-free hydrogen as an environmentally benign transportation fuel [4]. This paper presents the technical case for high-temperature hydrogen production processes. Large-scale efficient carbon-free hydrogen production can be accomplished by water splitting based on nuclear energy. Two candidate technologies are under consideration: thermochemical processes and high-temperature electrolysis, shown schematically in Fig. 1. The primary energy input for thermochemical processes is in the form of heat, whereas the primary energy input for high-temperature electrolysis is in the form of electricity. However, assuming the electricity is generated from a thermal energy source, both thermochemical and high-temperature electrolysis

processes can be analyzed as thermal water splitting processes.

Thermochemical processes comprise a series of thermally driven chemical reactions which have the net effect of water splitting with hydrogen and oxygen as products. The other reactants are recycled during the process. The most studied thermochemical process for nuclear hydrogen production is the sulfur-iodine (SI) process [5-6]. The sulfuric acid decomposition reaction in the SI process requires heat addition at a temperature of approximately 900°C. Active research activities on the SI process are under way in the US, France, and in Japan. Primary challenges include corrosion, catalyst degradation, and membranes separations.

High-temperature electrolysis utilizes a combination of thermal energy and electricity to split water in solid-oxide electrolysis cells (SOECs). These cells are similar to solid-oxide fuel cells (SOFCs). The feasibility of operating solid-oxide cells at high temperature in the electrolysis mode has been demonstrated for both tubular [7] and planar systems [8-9].

System modeling studies have been performed to compare the predicted overall hydrogen-production efficiency of the SI process with high-temperature electrolysis [10-11]. Results of these studies indicate similar expected performance for the two methods. However, high-temperature electrolysis faces fewer technical challenges to large-scale deployment.

NOMENCLATURE

F	Faraday number, 96487 C/mol
ASR	area-specific resistance, $\text{Ohm}\cdot\text{cm}^2$
ΔG_R	gibbs energy of reaction, J/mol
ΔH_f°	enthalpy of formation, J/mol
H_i	component sensible enthalpy, J/mol
ΔH_R	enthalpy of reaction, J/mol

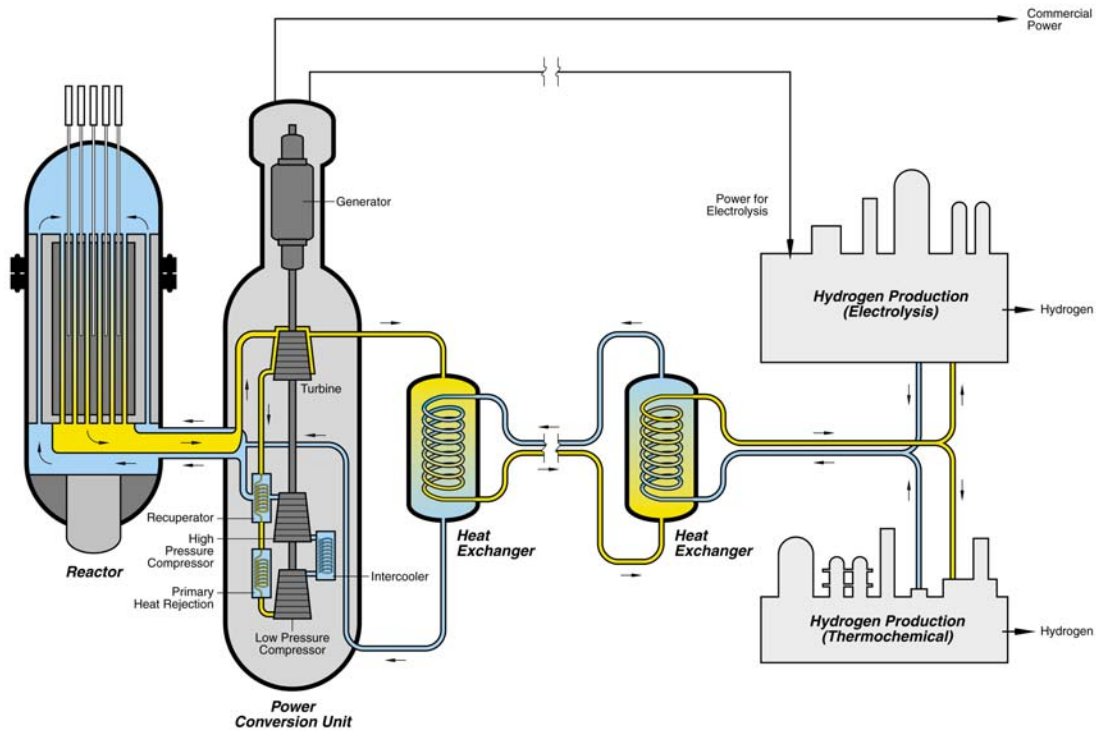


Figure 1. Nuclear hydrogen production concepts: thermochemical process and high-temperature electrolysis.

HHV	high heating value
i	current density, A/cm ²
I	current, A
j	number of electrons transferred per molecule of hydrogen produced
\dot{N}_{H_2}	molar hydrogen production rate, mol/s
P	pressure, kPa
q''	heat flux, W/cm ²
Q_H	high-temperature heat addition, J/mol
Q_L	low-temperature heat rejection, J/mol
\dot{Q}_T	isothermal heat transfer rate, W
\dot{Q}	heat transfer rate, W
R_u	universal gas constant, J/mol·K
ΔS_R	entropy of reaction, J/mol·K
T	temperature, K
T_o	standard temperature, K
T_L	temperature of heat rejection, K
T_H	temperature of heat addition, K
T_R	reactant temperature, K
T_P	product temperature, K
V°	standard-state open-cell potential, V
V_N	Nernst potential, V
V_{op}	operating voltage, V
V_{tn}	thermal neutral voltage, V
\dot{W}	work, rate basis, W
y	mole fraction
η_H	overall thermal-to-hydrogen efficiency
η_{th}	power cycle thermal efficiency
η_e	electrolysis efficiency

GENERAL THERMODYNAMICS OF THERMAL WATER SPLITTING

A basic thermodynamic analysis can be applied to a general thermal water-splitting process in order to determine the overall process efficiency limits as a function of temperature. Consider the process diagram shown in Fig. 2. Water enters the control volume from the left. Since the ultimate feedstock for any large-scale water-splitting operation will be liquid water, it is reasonable to consider the case in which water enters the control volume in the liquid phase at some temperature T and pressure P . Pure hydrogen and oxygen streams exit the control volume on the right, also at T and P . Two heat reservoirs are available, a high-temperature reservoir at temperature T_H and a low-temperature reservoir at temperature T_L . Heat transfer between these reservoirs and the control volume is indicated in the figure as Q_H and Q_L . Note that there is no work crossing the control-volume boundary. Therefore if the process under consideration is high-temperature electrolysis, both the power cycle (based on a heat engine for the purposes of this discussion) and the electrolyzer are located inside the control volume.

From a chemical reaction standpoint, the water-splitting process corresponds to the dissociation or reduction of water:



The first and second laws of thermodynamics can be applied to this process as follows:

$$1^{\text{st}} \text{ law:} \quad Q_H - Q_L = \Delta H_R \quad (2)$$

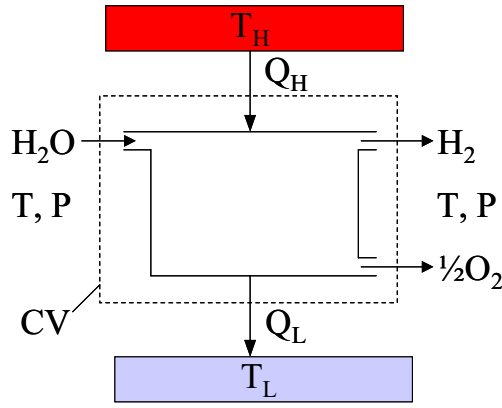


Figure 2. Schematic of a generic thermal water-splitting process operating between temperatures T_H and T_L .

2nd law:
$$\Delta S_R \geq \frac{Q_H}{T_H} - \frac{Q_L}{T_L} \quad (3)$$

where ΔH_R is the enthalpy of reaction and ΔS_R is the entropy change of the reaction. The overall thermal-to-hydrogen efficiency of thermal water splitting processes can be defined in terms of the net enthalpy increase of the reaction products over the reactants (can also be thought of as the energy content or heating value of the produced hydrogen), divided by the (costly) high-temperature heat added to the system:

$$\eta_H = \frac{\Delta H_R}{Q_H} \quad (4)$$

Combining the first and second law equations for the reversible case and substituting into the efficiency definition yields:

$$\eta_{H,\max} = \frac{1 - T_L/T_H}{1 - T_L \Delta S_R / \Delta H_R} \quad (5)$$

Note that the water splitting process defined in Fig. 2 is simply the reverse of the combustion reaction of hydrogen with oxygen. Therefore the enthalpy of reaction for the water-splitting process is the opposite of the enthalpy of combustion, which by definition is equal to the “heating value” of the hydrogen. Since for our process, we have assumed that the water enters the control volume in the liquid phase,

$$\Delta H_R = HHV \quad (6)$$

where HHV is the “high heating value” of hydrogen. If we further assume that T and P represent standard conditions, and that $T_L = T_o$,

$$\Delta H_R - T_L \Delta S_R = -\Delta G_{f,H_2O}^o \quad (7)$$

such that the efficiency expression can be rewritten as:

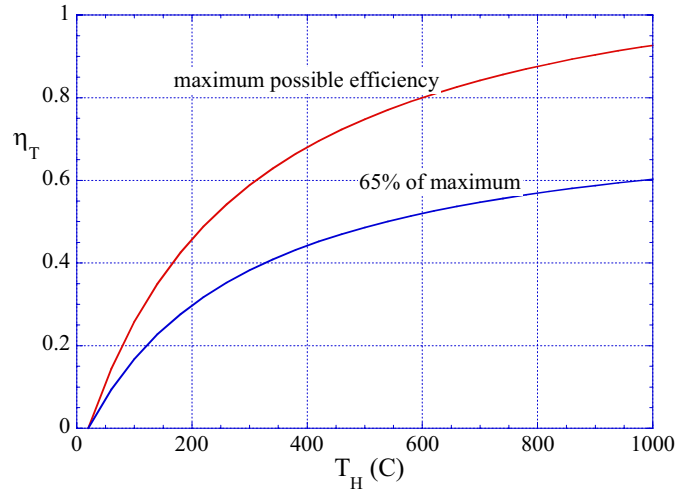


Figure 3. Theoretical thermal water splitting efficiencies.

$$\eta_{H,\max} = \left(1 - \frac{T_L}{T_H}\right) \left(\frac{HHV}{-\Delta G_{f,H_2O}^o} \right) = \left(1 - \frac{T_L}{T_H}\right) \left(\frac{1}{0.83} \right) \quad (8)$$

The high heating value of the hydrogen and the standard-state Gibbs energy of formation for water are fixed quantities such that the second factor on the right-hand side is a constant. This efficiency limit was also derived for the sulfur-iodine thermochemical process based on an exergy analysis in [12].

Comparing Eqn. (8) to Eqn. (4), the high-temperature heat requirement for the process can be stated as:

$$Q_H \geq \frac{T_H}{T_H - T_L} (-\Delta G_{f,H_2O}^o) \quad (9)$$

This result was derived for thermochemical cycles by Abraham and Schreiner [13], and applied to solar thermal dissociation of water by Fletcher and Moen [14], who noted that the maximum efficiencies of all thermochemical processes can be related to the efficiencies of Carnot engines operating between the same upper and lower temperatures. It is necessary only to add, conceptually, a reversible fuel cell which converts the hydrogen and oxygen to liquid water at the lower temperature, performing an amount of electrical work given by the Gibbs free energy of the reaction.

A plot of thermal water splitting efficiencies is presented in Fig. 3 for $T_L = 20^\circ\text{C}$. The top curve represents the maximum possible water-splitting efficiency result given by Eqn. (8). The bottom curve is simply 65% of this thermodynamic limit. The 65% value is based on a typical percentage of Carnot efficiency that can be achieved with a well engineered modern power cycle. The first conclusion to be drawn is that high temperature is needed for efficient hydrogen production based on thermal water splitting, regardless of the specific method used. If we assume that 65% of the maximum possible efficiency might also be achievable with a well engineered thermal water-splitting process, then

efficiencies of the magnitude given in the lower curve of Fig. 3 should be expected.

Detailed process analyses have been performed at INL [11] to analyze HTE-based hydrogen-production systems coupled to advanced nuclear reactors. Results from this study are presented in Fig. 4. This figure shows overall hydrogen production efficiencies, based on high heating value, plotted as a function of reactor outlet temperature. The figure includes a curve that represents 65% of the thermodynamic maximum efficiency, again assuming $T_L = 20^\circ\text{C}$. Three different advanced-reactor/power-conversion combinations were considered: a helium-cooled reactor coupled to a direct recuperative Brayton cycle, a supercritical CO_2 -cooled reactor coupled to a direct recompression cycle, and a sodium-cooled fast reactor coupled to a Rankine cycle. The system analyses were performed using UniSim [15] software. Each reactor/power-conversion combination was analyzed over an appropriate reactor outlet temperature range. The figure shows results for both HTE and low-temperature electrolysis (LTE). In addition, an efficiency curve for the SI thermochemical process is shown [16]. The results presented in Fig. 4 indicate that, even when detailed process models are considered, with realistic component efficiencies, heat exchanger performance, and operating conditions, overall hydrogen production efficiencies in excess of 50% can be achieved for HTE with reactor outlet temperatures above 850°C . For reactor outlet temperatures of $600 - 800^\circ\text{C}$, the supercritical CO_2 /recompression power cycle is superior to the He-cooled/Brayton cycle concept. This conclusion is consistent with results presented in [17]. The efficiency curve for the SI process also includes values above 50% for reactor outlet temperatures above 900°C , but it drops off quickly with decreasing temperature, and falls below values for LTE coupled to high-temperature reactors for outlet temperatures below 800°C . Even LTE benefits from higher reactor outlet temperatures because of the improved power conversion thermal efficiencies. Current planning for NGNP [18] indicates that reactor outlet temperatures will be at or below 900°C , which favors HTE

THERMODYNAMICS OF HIGH TEMPERATURE ELECTROLYSIS

Focusing now on electrolysis, consider a control volume surrounding an isothermal electrolysis process, as shown in Fig. 5. In this case both work and heat interactions cross the control volume boundary. The first law for this process is given by:

$$Q - W = \Delta H_R \quad (10)$$

For reversible operation,

$$Q_{rev} = T\Delta S_R \quad (11)$$

Such that

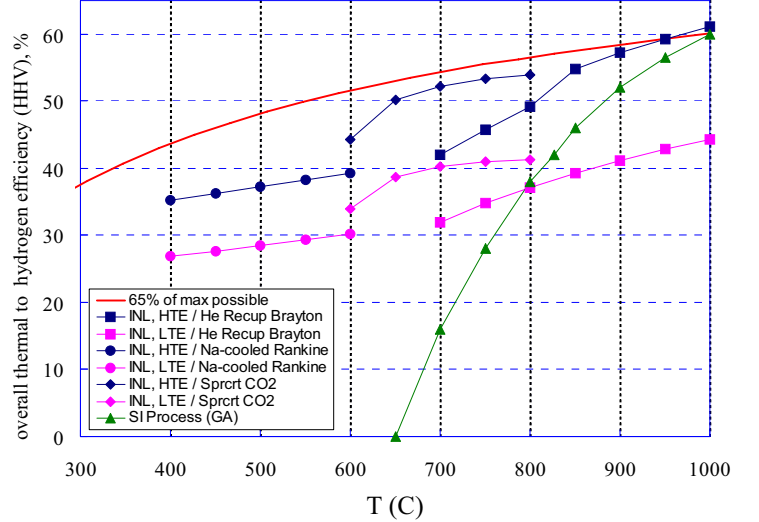


Figure 4. Overall thermal-to-hydrogen efficiencies for HTE coupled to three different reactor types, as a function of reactor outlet temperature.

$$W_{rev} = \Delta H_R - T\Delta S_R = \Delta G_R \quad (12)$$

The thermodynamic properties appearing in Eqn. (12) are plotted in Fig. 6 as a function of temperature for the $\text{H}_2\text{-H}_2\text{O}$ system from 0°C to 1000°C at standard pressure. This figure is often cited as a motivation for high-temperature electrolysis versus low-temperature electrolysis. It shows that the Gibbs free energy change, ΔG_R , for the reacting system decreases with increasing temperature, while the product of temperature and the entropy change, $T\Delta S_R$, increases. Therefore, for reversible operation, the electrical work requirement decreases with temperature, and a larger fraction of the total energy required for electrolysis, ΔH_R , can be supplied in the form of heat. Since heat-engine-based electrical work is subject to a production thermal efficiency of typically 50% or lower, decreasing the work requirement results in higher overall thermal-to-hydrogen production efficiencies. Note that the total energy requirement, ΔH_R , increases only slightly with temperature, and is very close

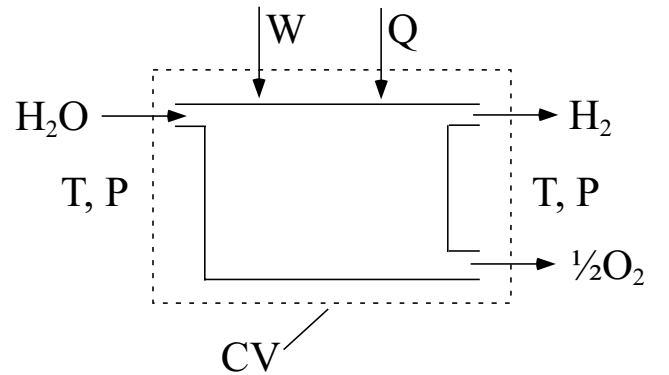


Figure 5. Schematic of a water electrolysis process operating at temperature T .

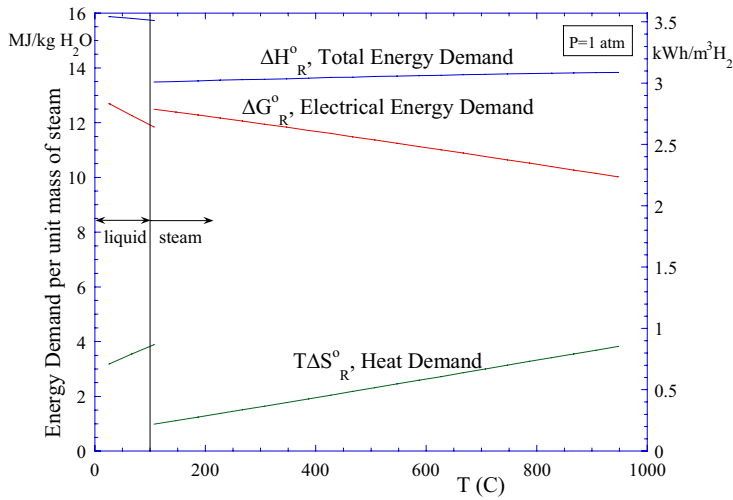


Figure 6. Standard-state energy requirements for electrolysis as a function of temperature.

in magnitude to the lower heating value of hydrogen. The ratio of ΔG_R to ΔH_R is about 93% at 100°C and about 70% at 1000°C. Operation of the electrolyzer at high temperature is also desirable from the standpoint of reaction kinetics and electrolyte conductivity, both of which improve dramatically at higher operating temperatures. Potential disadvantages of high-temperature operation include the limited availability of very high temperature process heat and materials issues such as corrosion and degradation.

The solid-oxide electrolysis cell is a solid-state electrochemical device consisting of an oxygen-ion-conducting electrolyte (e.g., yttria- or scandia-stabilized zirconia) with porous electrically conducting electrodes deposited on either side of the electrolyte. A cross-section of a planar design is shown in Fig. 7. The design depicted in the figure shows an electrolyte-supported cell with a nickel cermet cathode and a perovskite anode such as strontium-doped lanthanum manganite (LSM). In an electrolyte-supported cell, the electrolyte layer is thicker than either of the anodes. The flow fields conduct electrical current through the stack and provide flow passages for the process gas streams. The separator plate or bipolar plate separates the process gas streams. It must also be electrically conducting and is usually metallic, such as a ferritic stainless steel. A wealth of information on materials, configurations, and designs of solid-oxide electrochemical systems is available in reference [19].

As shown in the figure, a mixture of steam and hydrogen at 750-950°C is supplied to the cathode side of the electrolyte (note that cathode and anode sides are opposite to their fuel-cell-mode roles). The half-cell electrochemical reactions occur at the triple-phase boundary near the electrode/electrolyte interface, as shown in the figure. Oxygen ions are drawn through the electrolyte by an applied electrochemical potential. The ions liberate their electrons and recombine to form molecular O_2 on the anode side. The inlet steam-hydrogen mixture composition may be as much as 90% steam, with the remainder hydrogen. Hydrogen is included in the inlet stream

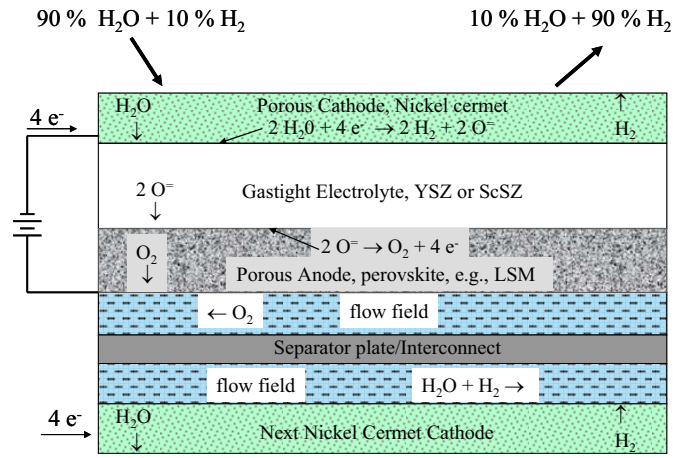


Figure 7. Cross-section of a planar high temperature electrolysis stack.

in order to maintain reducing conditions at the cathode. The exiting mixture may be as much as 90% H_2 . Product hydrogen and residual steam is passed through a condenser or membrane separator to purify the hydrogen.

In order to accomplish electrolysis, a voltage must be applied across the cell that is greater than the open-cell potential. The standard-state open-cell potential is given by:

$$V^o = \frac{\Delta G_R^o}{jF} \quad (13)$$

where j is the number of electrons transferred per molecule of hydrogen produced. For the steam-hydrogen system, $j=2$, as indicated in Fig. 7 in which the O^- ions are transported through the solid-oxide electrolyte. The standard-state open-cell potential applies to the case in which pure reactants and products are separated and at one standard atmosphere pressure. In most practical HTE systems, the incoming steam is mixed with some hydrogen and possibly some inert gas. Using the material set shown in Fig. 7, inlet hydrogen is required in order to maintain reducing conditions on the nickel cermet electrode. Also, it is not desirable to run the electrolyzer to 100% steam utilization, because localized steam starvation will occur, severely degrading performance. Therefore, the outlet stream will include both steam and hydrogen. Residual steam can be removed from the product by condensation. On the oxygen-evolution side of the cells, air is often used as a sweep gas, so the oxygen partial pressure is only about 21% of the operating pressure. In addition, the electrolysis system can operate at elevated pressure. In order to account for the range of gas compositions and pressures that occur in a real system, the open-cell (or Nernst) potential can be obtained from the Nernst equation, which can be written as:

$$V_N = V^o - \frac{R_u T}{jF} \ln \left[\left(\frac{y_{H_2O}}{y_{H_2} y_{O_2}^{1/2}} \right) \left(\frac{P}{P_{std}} \right)^{-1/2} \right] \quad (14)$$

Operation of a solid-oxide stack in the electrolysis mode is fundamentally different than operation in the fuel-cell mode for several reasons, aside from the obvious change in direction of the electrochemical reaction. From the standpoint of heat transfer, operation in the fuel-cell mode typically necessitates the use of significant excess air flow in order to prevent overheating of the stack. The potential for overheating arises from two sources: (1) the exothermic nature of the hydrogen oxidation reaction, and (2) ohmic heating associated with the electrolyte ionic resistance and other loss mechanisms.

Conversely, in the electrolysis mode, the steam reduction reaction is endothermic. Therefore, depending on the operating voltage, the net heat generation in the stack may be negative, zero, or positive. This phenomenon is illustrated in Fig. 8. The figure shows the respective internal heat sink/source fluxes in a planar solid-oxide stack associated with the electrochemical reaction and the ohmic heating. The ohmic heat flux (W/cm^2) is given by:

$$q''_{Ohm} = i^2 ASR = i(V_{op} - V_N) \quad (15)$$

where i is the current density (A/cm^2) and V_N is the mean Nernst potential for the operating cell. The reaction heat flux is given by:

$$q''_R = \frac{i}{2F} (T\Delta S_e) = \frac{i}{2F} (\Delta G_e - \Delta H_R) \quad (16)$$

where ΔS_e is the entropy change for the actual electrolysis process, accounting for the reactant and product partial pressures.

The net heat flux is also shown in Fig. 8. An area-specific resistance of 1.25, an operating temperature of 1200 K, and hydrogen mole fractions of 0.1 and 0.95 at the inlet and outlet, respectively, were assumed for these calculations. In the fuel-cell mode, the net heat flux is always positive and increases rapidly with operating voltage and current density. In the electrolysis mode, the net heat flux is negative for low operating voltages, increases to zero at the “thermal-neutral” voltage, and is positive at higher voltages and current densities. The thermal-neutral voltage can be predicted from direct application of the rate-based First Law to the isothermal system shown in Fig. 5:

$$\dot{Q} - \dot{W} = \Delta \dot{N}_{H_2} \Delta H_R \quad (17)$$

where, from Faraday’s law,

$$\Delta \dot{N}_{H_2} = I / 2F \quad (18)$$

Letting $\dot{Q} = 0$ (no external heat transfer), $\dot{W} = IV_m$, yielding:

$$V_m = \Delta H_R / 2F \quad (19)$$

Note that the reaction heat flux of Eqn. (16) can also be written in terms of the thermal-neutral voltage as:

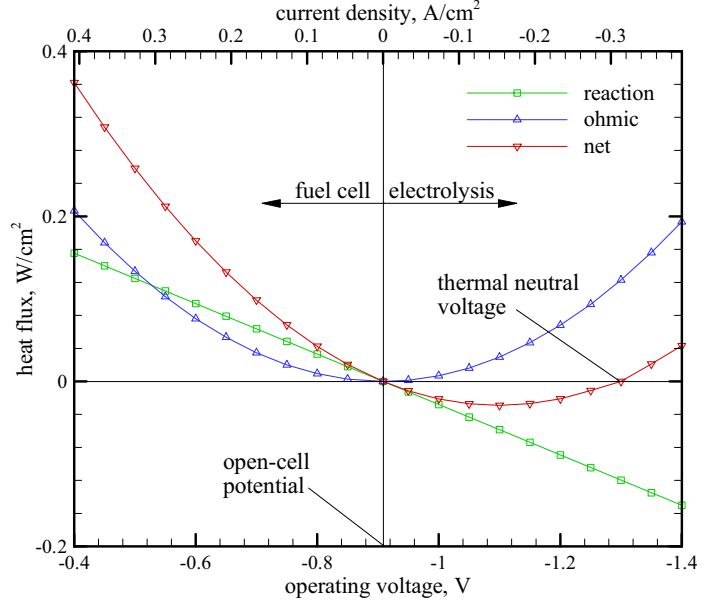


Figure 8. Thermal contributions in electrolysis and fuel cell modes of operation.

$$q''_R = i(V_N - V_m) \quad (20)$$

Since the enthalpy of reaction, ΔH_R , is strictly a function of temperature (ideal gas approximation), the thermal-neutral voltage is also strictly a function of temperature, independent of cell ASR and gas compositions. The particular values of net cell heat flux at other operating voltages do however depend on cell ASR and gas compositions. The thermal-neutral voltage increases only slightly in magnitude over the typical operating temperature range for solid-oxide cells, from 1.287 V at 800°C to 1.292 V at 1000°C. At typical solid-oxide electrolysis stack temperatures and ASR values, operation at the thermal-neutral voltage yields current densities in the 0.2 – 0.6 A/cm^2 range, which is very close to the current density range that has yielded successful long-term operation in solid-oxide fuel cell stacks.

Operation at or near the thermal-neutral voltage simplifies thermal management of the stack since no significant excess gas flow is required and component thermal stresses are minimized. In fact, in the electrolysis mode, since oxygen is being produced, there is also no theoretical need for air flow to support the reaction at all. In a large-scale electrolysis plant, the pure oxygen produced by the process could be saved as a valuable commodity. However, there are several good reasons to consider the use of a sweep gas on the oxygen side. First, the use of a sweep gas will minimize the performance degradation associated with any small leakage of hydrogen from the steam/hydrogen side to the oxygen side of the cell. Second, there are serious materials issues associated with the handling of pure oxygen at elevated temperatures. Finally, the use of a sweep gas (especially one that does not contain oxygen) on the oxygen side of the electrolysis cell reduces the average mole fraction and partial pressure of oxygen, thereby

reducing the open-cell and operating potentials, resulting in higher electrolysis efficiencies, as we shall see shortly.

There are some additional thermodynamic implications related to the thermal neutral voltage. In particular, electrolyzer operation at or above the thermal neutral voltage negates the argument that is often stated as a motivation for high-temperature electrolysis that a fraction of the total energy requirement can be supplied in the form of heat. In fact, for isothermal operation at voltages greater than thermal neutral, heat rejection is required.

Electrolysis efficiency, η_e , can be defined for HTE, analogous to the definition of fuel cell efficiency [20]. The electrolysis efficiency quantifies the heating value of the hydrogen produced by electrolysis per unit of electrical energy consumed in the stack. Based on this definition,

$$\eta_e = \frac{\dot{N}_{H_2} \Delta H_R}{VI} \quad (21)$$

and since the stack electrical current is directly related to the molar production rate of hydrogen via Faraday's law, the electrolysis efficiency can be expressed strictly in terms of cell operating potentials as:

$$\eta_e = \frac{\Delta H_R / 2F}{V_{op}} = \frac{V_{tn}}{V_{op}} \quad (22)$$

The efficiency for the fuel-cell mode of operation is the inverse of Eqn. (22). A fuel utilization factor is often included in the fuel-cell efficiency definition, but it is not needed in the electrolysis definition since no fuel (only steam) is wasted at low utilization.

It should be noted that the value of the efficiency defined in this manner for electrolysis is greater than 1.0 for operating voltages lower than thermal neutral. As an example, for the reversible standard-state reference case, from Eqn. (12), on a rate basis:

$$\dot{W}_{rev} = \dot{N}_{H_2} \Delta G_R^o = IV^o \quad (23)$$

Invoking Faraday's law, the operating cell potential for this case approaches the reference open-cell value, $V^o = \Delta G_R / 2F$, yielding:

$$\eta_{e,o} = \frac{\Delta H_R^o}{\Delta G_R^o} \quad (24)$$

which for steam electrolysis at 850°C is equal to 1.34. For cases with variable gas composition or partial pressure, the open-cell potential is given by the Nernst Equation (14) and the corresponding efficiency limit varies accordingly. It is not desirable to operate an electrolysis stack near the efficiency limit, however, because the only way to approach this limit is to operate with very low current density. There is a trade-off between efficiency and hydrogen production rate in selecting an electrolysis stack operating voltage. This trade-off is illustrated in Fig. 9. The upper curve in the figure shows the

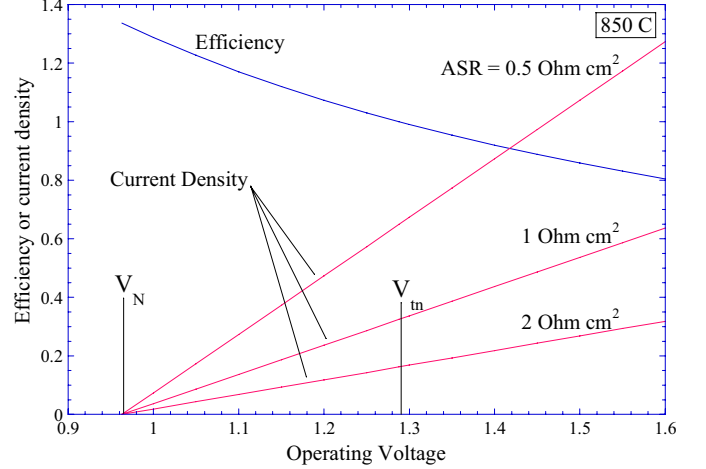


Figure 9. Effect of operating voltage and area-specific resistance on electrolysis efficiency.

decrease in electrolysis efficiency that occurs as the per-cell operating voltage is increased above the open-cell voltage, V_N , according to Eqn. (22). Operation at the thermal-neutral voltage yields an electrolysis efficiency of 1.0. Area-specific resistance (ASR) represents the net effect of all the loss mechanisms in the electrolysis stack including, ohmic losses, activation and concentration overpotentials, etc. The bottom curves show the effect of operating voltage and ASR on the current density. Noting that:

$$V_{op} = \bar{V}_N + i \times ASR, \quad (25)$$

if a target current density (and corresponding hydrogen production rate) is selected, lower ASR values allow for stack operation at lower voltages and correspondingly higher efficiencies. Similarly, in the fuel-cell mode, there is a tradeoff between efficiency and maximum power production. Maximum power production for solid-oxide fuel cells occurs for operation at around 0.5 V, whereas maximum efficiency occurs at the open-cell potential, around 1.1 V for hydrogen-dominated SOFC fuel cell inlet gas compositions. Depending on cell performance and optimization parameters, a good operating point usually occurs at around 0.7 V in the fuel-cell mode of operation. In the electrolysis mode, a good tradeoff between efficiency and hydrogen production rate will occur at operating voltages below $\Delta H_R / 2F$, around 1.1 V. The challenge is to develop SOEC stacks with low ASR such that a reasonable current density will be achievable at lower operating voltages. Low operating voltages can also be maintained at a specified current density if the mean Nernst potential, \bar{V}_{Nernst} , is low. The mean Nernst potential can be reduced by increasing the cell operating temperature, increasing the steam content and flow rate in the feed stream, or by decreasing the oxygen content on the sweep gas side (anode) of the electrolysis cell. Of course, as the cell current density and hydrogen production rate is increased, the average steam content on the cathode side decreases and the average oxygen content on the anode side

increases. These considerations indicate that, for maximum cell efficiency at a specified current density, steam utilization should be kept low and a high flow rate of a non-oxygen-containing sweep gas should be used. Unfortunately, results of large-scale system analyses [21] show that operating with low steam utilization results in low overall hydrogen production system efficiencies. For the system, the thermodynamic benefit of excess steam (lower average Nernst potential) is outweighed by the penalties associated with handling of the excess steam and incomplete heat recuperation. Similar conclusions were drawn when considering the use of a non-oxygen-containing sweep gas (e.g., steam) on the oxygen side. Again, the thermodynamic benefits were outweighed by system considerations. In fact, the highest overall efficiencies for pressurized electrolyzers were achieved with no sweep gas, where the oxygen is allowed to evolve from the cells undiluted.

ISOTHERMAL VS. NON-ISOTHERMAL OPERATION

The analyses presented so far have all assumed isothermal electrolysis operation such that the outlet temperature of the products is the same as the inlet temperature of the reactants. For operating voltages between the open-cell potential and thermal neutral, isothermal operation requires heat addition during the electrolysis process. For operating voltages above thermal neutral, heat rejection is required to maintain isothermal operation. The enthalpy change for the electrolysis process under isothermal conditions is, by definition, the “enthalpy of reaction,” ΔH_R . The enthalpy of reaction for steam reduction is a weak function of temperature, with a numerical value very close to the low heating value of hydrogen over a wide range of temperatures, as shown in Fig. 6. The magnitude of the heat transfer required to achieve isothermal operation, $\dot{Q}_T(T)$, can be calculated directly from the following form of the first law:

$$\dot{Q}_T(T) = \Delta \dot{N}_{H_2} \Delta H_R(T) - IV_{op} \quad (26)$$

and since the hydrogen production rate, $\Delta \dot{N}_{H_2}$ is equal to $I/2F$, and the thermal neutral voltage, $V_m = \Delta H_R(T)/2F$,

$$\dot{Q}_T(T) = I(V_m - V_{op}) \quad (27)$$

Note that this result predicts positive heat transfer to the electrolyzer for operating voltages less than thermal neutral and negative heat transfer (i.e., heat rejection from the electrolyzer) for operating voltages greater than thermal neutral. Since there is no sensible enthalpy change, this result is valid for all isothermal cases, even if excess reactants and/or inert gases are present. A graphical interpretation of the isothermal heat requirement on V-i coordinates is shown in Fig. 10. The figure shows the heat fluxes required to maintain isothermal operation for a target current density of 0.3 A/cm² for two values of ASR: 0.5 and 1.5 Ohm·cm² represented by the area enclosed between the vertical line at $V = V_m$, the vertical line $V = V_{op}$ ($V_{op} =$

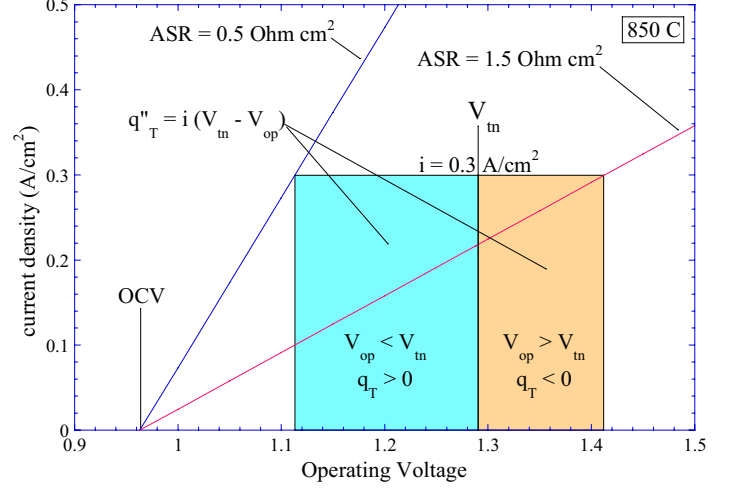


Figure 10. Graphical interpretation of isothermal heat requirements for two values of ASR.

1.113 V for $ASR = 0.5 \text{ Ohm}\cdot\text{cm}^2$; $V_{op} = 1.413 \text{ V}$ for $ASR = 1.5 \text{ Ohm}\cdot\text{cm}^2$), and the horizontal lines at $i = 0$ and at $i = 0.3 \text{ A/cm}^2$. Note that the higher ASR case requires an operating voltage that is above V_m in order to achieve the target current density of 0.3 A/cm². Consequently, the associated isothermal heat transfer requirement is negative, indicating that heat rejection is needed to maintain isothermal operation at that condition.

Eqn. (27) can also be used to show that the maximum isothermal heat addition operating point corresponds to an operating voltage equal to the average of the open-cell potential and the thermal neutral voltage. Accordingly, the maximum isothermal heat addition is given by:

$$\dot{Q}_{\max}(T) = I \left(\frac{V_m - V_N}{2} \right) \quad (28)$$

where V_N is the open-cell potential. The total stack current, I , at any operating voltage is dependent on the stack ASR value, which is typically temperature-dependent.

Actual high-temperature electrolysis processes will generally not operate isothermally unless the operating voltage is very close to the thermal neutral voltage. For non-isothermal cases, the first law for electrolysis process must be written as:

$$\dot{Q} - \dot{W} = \sum_P \dot{N}_i [\Delta H_{f_i}^o + H_i(T_P) - H_i^o] - \sum_R \dot{N}_i [\Delta H_{f_i}^o + H_i(T_R) - H_i^o] \quad (29)$$

In this form, all reacting and non-reacting species included in the inlet and outlet streams can be accounted for, including inert gases, inlet hydrogen (introduced to maintain reducing conditions on the steam/hydrogen electrode), and any excess unreacted steam. In general, determination of the outlet temperature from Eqn. (29) is an iterative process [22]. The heat transferred during the process must first be specified (e.g., zero for the adiabatic case). The temperature-dependent enthalpy values of all species must be taken into account. The

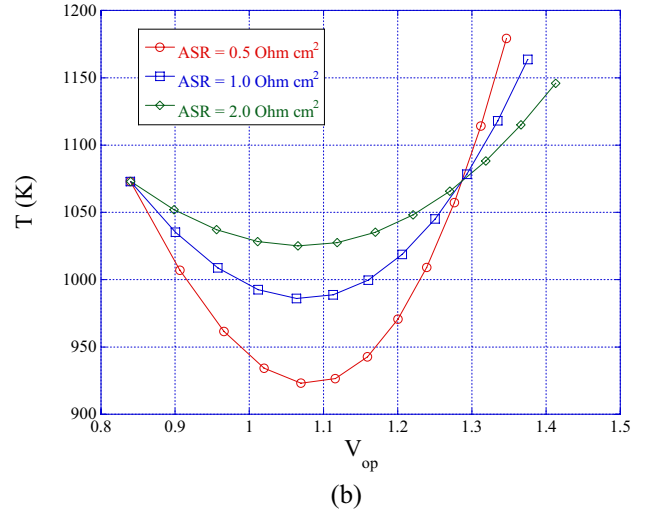
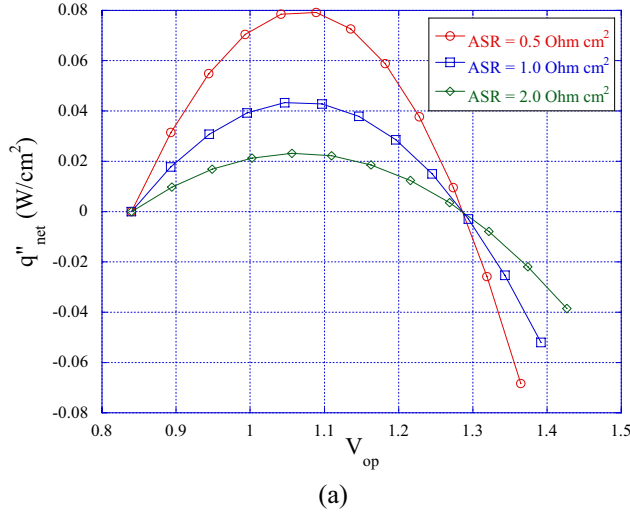


Figure 11. (a) Heat flux required for isothermal operation; (b) Outlet temperature for adiabatic operation; steam-hydrogen inlet flow rate: 0.0085 gm/min/cm², $y_{H_2i} = 0.1$, sweep air inlet flow rate: 0.00561 gm/min/cm², $T_{in} = 1073$ K.

solution procedure begins with specification of the cathode-side inlet flow rates of steam, hydrogen, and any inert carrier gas such as nitrogen (if applicable). The inlet flow rate of the sweep gas (e.g., air or steam) on the anode side must also be specified. Specification of these flow rates allows for the determination of the inlet mole fractions of steam, hydrogen, and oxygen that appear in the Nernst equation. The steam mole fraction is expressed in terms of the hydrogen mole fraction as $1 - y_{H_2} - y_{N_2}$. The desired current density and active cell area are then specified, yielding the total operating current. The corresponding hydrogen production rate is obtained from Faraday's law.

Once the per-cell hydrogen production rate is known, the outlet flow rates of hydrogen and steam on the cathode side and oxygen on the anode side can be determined. The flow rates of any inert gases, the anode-side sweep gas, and any excess steam or hydrogen are the same at the inlet and the outlet. Once all these flow rates are known, the summations in Eqn. (29) can be evaluated. The product summation must be evaluated initially at a guessed value of the product temperature, T_p .

The operating voltage corresponding to the specified current density is obtained from Eqn. (25), where the stack area-specific resistance, ASR , must be estimated and specified as a function of temperature. To account for the variation in temperature and composition across an operating cell, the mean Nernst potential can be obtained from an integrated version of the Nernst equation:

$$\bar{V}_N = \frac{1}{2F(T_p - T_R)(y_{o,O_2,A} - y_{i,O_2,A})(y_{o,H_2,C} - y_{i,H_2,C})} \times \int_{T_R}^{T_p} \int_{y_{i,O_2,A}}^{y_{o,O_2,A}} \int_{y_{i,H_2,C}}^{y_{o,H_2,C}} \Delta G_R(T) + R_u T \ln \left(\frac{1 - y_{H_2} - y_{N_2}}{y_{H_2} y_{O_2}^{1/2}} \right) dy_{H_2} dy_{O_2} dT \quad (30)$$

where $y_{i,O_2,A}$ is the anode-side inlet mole fraction of oxygen, etc. Note that the upper limit of integration on the temperature integral is initially unknown. Once the ASR and the mean Nernst potential are known, the operating voltage is obtained from Eqn. (25) and the electrical work term in Eqn. (29) is obtained from $\dot{W} = -V_{op}I$. An algorithm then must be developed to iteratively solve for the product temperature, T_p , in order to satisfy Eqn. (29).

Results of sample parametric calculations based on this procedure are presented in Fig. 11. The inlet mass flow rates of steam-hydrogen and sweep air per cm² of active cell area are indicated in the caption. The calculations were performed for an inlet hydrogen mole fraction of 0.1 and an inlet temperature of 800°C (1073 K). Fig. 11(a) shows the heat flux required to maintain isothermal operation as a function of per-cell operating voltage for three different ASR values. This heat flux is positive (heat addition required) for voltages between open-cell and thermal neutral and negative for higher operating voltages. The peak heat flux requirement occurs halfway between the open-cell potential and the thermal neutral voltage. The magnitude of the peak heat flux is highest for the lowest ASR value since the current density (and hydrogen production rate) corresponding to each voltage value is highest for the lowest ASR value. Fig. 11(b) shows the mean outlet gas temperature as a function of per-cell operating voltage for adiabatic operation for three different ASR values. For adiabatic conditions, outlet temperatures are lower than inlet temperatures for voltages between open-cell and thermal neutral. For higher voltages, outlet temperatures increase rapidly with voltage. Again, the low- ASR case exhibits the largest effect due to its higher current density at each operating voltage.

Actual electrolyzers will generally operate at conditions that are neither isothermal, nor adiabatic. These two cases represent limits. For optimal performance, isothermal operation at an operating voltage below thermal neutral is

desirable. In this case, some of the electrolysis energy is indeed supplied in the form of heat. One way to supply the required heat directly to the stack is through the use of a heated sweep gas.

DIFFERENT HEAT ADDITION TEMPERATURES FOR THE POWER CYCLE AND THE ELECTROLYZER

Since the primary energy input to a high-temperature electrolyzer is electrical work, the electrolyzer does not necessarily have to be directly coupled to the same heat source used for the power cycle. If we wish to focus on water-splitting by electrolysis, and we are interested in determining the overall thermal-to-hydrogen efficiency limits for a wide range of cases, we can start by drawing a control volume around the combination of the power cycle and the electrolyzer, as shown in Fig. 12. The figure also shows two individual control volumes, CV1 and CV2 around the power cycle and the electrolyzer, respectively. According to the schematic, we are allowing for the possibility that the heat addition temperature for the power cycle may be different than the heat addition temperature for the electrolyzer. Note that the work produced by the power cycle is fed directly to the electrolyzer and that no work crosses the combined control-volume boundary (CV1+CV2). Applying the overall thermal-to-hydrogen efficiency definition to the combined control volume,

$$\eta_H = \frac{\Delta H_R}{Q_{Tot}} = \frac{\Delta H_R}{Q_{H,P} + Q_{H,e}} \quad (31)$$

And noting that for the ideal case,

$$Q_{H,P} = \frac{W_{net}}{\eta_{th}} = \frac{\Delta H_R}{\eta_{th} \eta_e}; Q_{H,e} = T_{H,e} \Delta S_R(T_{H,e}) \quad (32)$$

we obtain:

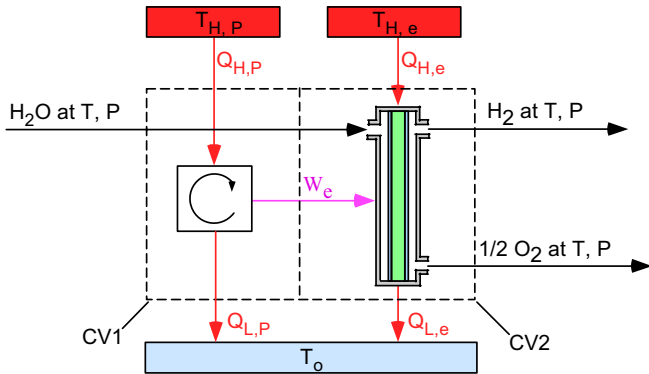


Figure 12. Schematic for determination of overall thermal-to-hydrogen efficiency for an electrolysis process.

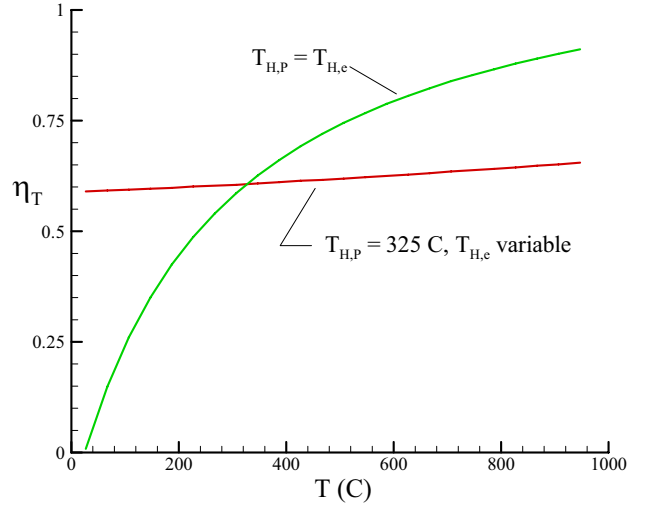


Figure 13. Ideal thermal-to-hydrogen efficiencies for variable and fixed values of $T_{H,P}$.

$$\eta_H = \frac{\Delta H_R}{\frac{\Delta H_R}{\eta_{th} \eta_e} + T_{H,e} \Delta S_R(T_{H,e})} \quad (33)$$

If the initial and final temperature and pressure are designated to be equal to the standard-state reference values, $T=T_o$, $P=P_o$, the enthalpy change of the electrolysis reaction is the same as the heating value of the hydrogen produced. Since the feedstream at T_o and P_o would be in the liquid phase, the process efficiency should be defined in terms of the high heating value, HHV. But the low heating value, LHV, could also be used. Using the high heating value,

$$\eta_H = \frac{HHV}{\frac{HHV}{\eta_{th,P} \eta_e} + T_{H,e} \Delta S_R(T_{H,e})} \quad (34)$$

Separate consideration of the First Law and Second Law to CV1 and CV2 yields the maximum possible thermal efficiency of the power cycle (i.e., Carnot) and the maximum possible electrolysis efficiency:

$$\eta_{th,P,max} = 1 - \frac{T_L}{T_{H,P}}; \quad \eta_{e,max} = \frac{HHV}{HHV - \Delta S_R(T_{H,e}) \cdot (T_{H,e} - T_L) - T_L \Delta S_R(T_L)} \quad (35)$$

where $\Delta S_R(T_H)$ is the entropy change for the electrolysis reaction evaluated at T_H and $\Delta S_R(T_L)$ is the entropy change for the reaction evaluated at T_L . It should be noted that the

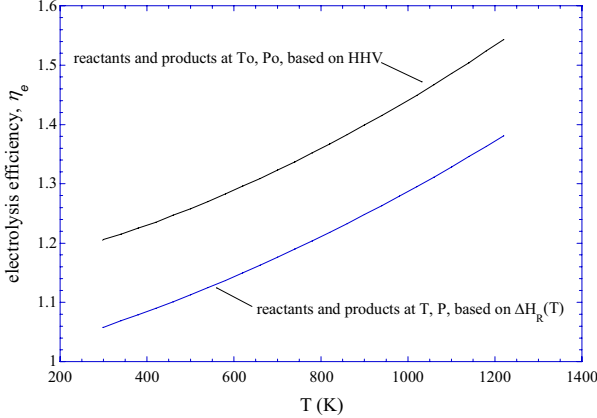


Figure 14. Maximum possible electrolysis efficiencies plotted as a function of the heat source temperature, $T_{H,e}$.

ideal overall thermal-to-hydrogen efficiency, η_T , predicted by Eqns. (34) and (35) yields the same values as those predicted by Eqn. (8), shown in Fig. 3, if the heat addition temperatures for the power cycle, $T_{H,P}$, and the electrolysis process, $T_{H,e}$, are equal. Eqns. (8) and (34) can be shown to be equivalent algebraically as well, again for the case of $T_H = T_{H,P} = T_{H,e}$. This maximum possible water splitting efficiency is reproduced in Fig. 13, for the case of variable $T_{H,P} = T_{H,e}$. If we are interested in the case of $T_{H,P} < T_{H,e}$, such as the case in which the high-temperature electrolysis process is driven by a conventional power cycle (e.g., a PWR driving a rankine cycle) that has a lower temperature of heat addition than the electrolysis operating temperature, then Eqn. (34) can still be used to evaluate the ideal overall thermal-to-hydrogen efficiency. For example, if we let $T_{H,P} = 325^\circ\text{C}$, and allow $T_{H,e}$ to be a variable, Eqn. (20) yields the second result shown in Fig. 13. This efficiency curve has a much shallower slope, implying that the potential gains to be realized from high-temperature electrolysis are modest, if the power-cycle heat addition temperature (and thermal efficiency) is fixed. Note that the low-temperature end of this curve corresponds to the efficiency limit for conventional low-temperature electrolysis with a 325°C temperature of heat addition for the power cycle. Actual low-temperature electrolysis overall efficiency values are typically around 35%, which is close to 65% of the low-temperature thermodynamic limit shown in the figure.

A plot of the thermodynamic limits for electrolysis efficiency, η_e , given by Eqn. (35), for $T_L = T_o$, $P = P_o$, is presented in the top curve of Fig. 14 as a function of the heat source temperature, $T_{H,e}$. This figure also shows the electrolysis efficiency limit given by Eqn. (24), which corresponds to $T = T_{H,e}$, $P = P_o$ and is based on the enthalpy of reaction at the electrolysis temperature, ΔH_R . Again, these limits can only be approached when operating near the Nernst potential, with correspondingly low current densities. But the curves do illustrate the potential advantage of high temperature operation. Note that these electrolysis efficiency curves have a steeper slope with respect to temperature than the overall thermal-to-hydrogen efficiency curve shown in Fig. 13 for the

case of a fixed power-source heat-addition temperature. This is because the electrolysis efficiency simply quantifies the hydrogen generation rate per unit of electrical power consumed. It does not account for any additional **net** heat requirement (a large percentage of the required heating can be recuperated) that might be associated with boosting the steam up to the final electrolysis temperature. For example, if the final temperature boost is achieved through electrical resistance heating, the power consumed in the heater would have to be taken into account in evaluating the overall power-to-hydrogen efficiency.

We can also derive an expression for the overall hydrogen production efficiency as a function of the operating voltage for an electrolysis process. For this case, consider control volume CV2 of Fig. 12 and let $W_e = VI$. For a control volume drawn around the electrolysis stack, with inlet and outlet streams at T , P , direct application of the first law and the definition of the overall thermal-to-hydrogen efficiency yields:

$$\eta_H = \frac{\Delta H_R}{2FV_{op}(1/\eta_{th} - 1) + \Delta H_R} \quad (36)$$

Note that at $V_{op} = V_m$, this result yields $\eta_T = \eta_P$. So operation at the thermal neutral voltage yields the same overall hydrogen production efficiency as that of the power cycle. Letting $V_{op} = V^\circ$, Eqn. (36) yields

$$\eta_{H,V^\circ} = \frac{\eta_{th}\Delta H_R}{\Delta G_R(1 - \eta_{th}) + \eta_{th}\Delta H_R} \quad (37)$$

which is the overall efficiency corresponding to operation at the reference potential, V° . This efficiency is always higher than the power-production thermal efficiency. The open-cell potential corresponding to the electrolyzer operating conditions, including temperature and gas partial pressures, is given by the Nernst equation, Eqn (14). For a specified temperature, the open-cell potential is lower than V° for high steam mole fraction, low hydrogen mole fraction, low oxygen mole fraction, and low operating pressure. For electrolysis, it is desirable to have as low an open-cell potential as possible, since the operating cell current density is proportional to the difference between the operating voltage and the open-cell voltage. If the open-cell voltage is low, a reasonable current density can be achieved with a low operating voltage, and therefore with high efficiency, according to Eqn. (36). The effect of operating potential on overall thermal-to-hydrogen efficiency is illustrated in Fig. 15. This figure shows a series of overall efficiency curves, over a range of assumed power-production efficiency values for an electrolysis temperature of 800°C . Note that operating at any voltage lower than thermal neutral yields a hydrogen-production efficiency that is greater than the power-cycle thermal efficiency. On the steam/hydrogen side of the electrolysis cell, the use of high inlet steam mole fraction and a high total steam flow rate is desirable, subject to the constraint that a hydrogen content of 5

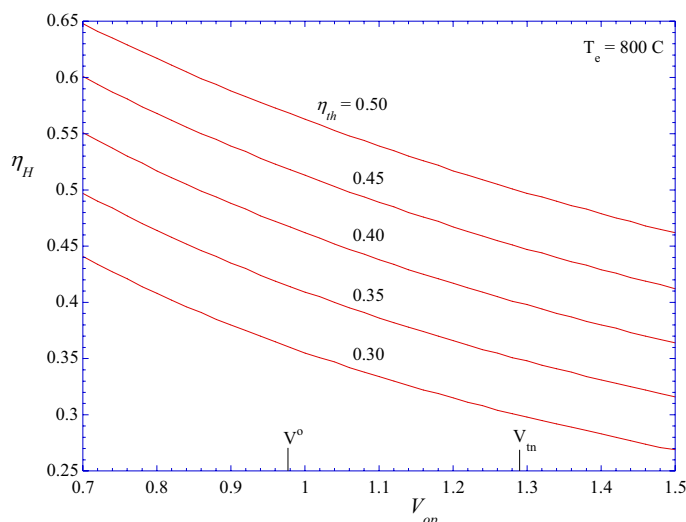


Figure 15. Overall hydrogen production efficiencies as a function of power-production thermal efficiency and electrolyzer per-cell operating voltage.

– 10% must be used in order to maintain reducing conditions on the steam/hydrogen electrode. On the oxygen side, a low average oxygen mole fraction is desirable. Therefore, a non-oxygen-containing sweep gas should be used with a high flow rate. As discussed, previously, however, these thermodynamic effects can be outweighed by other system considerations such as incomplete heat recuperation, handling of excess non-reacted steam, compression work for sweep gases, etc., when performing detailed system analyses with realistic component efficiencies and heat exchanger characteristics.

As an example HTE operating condition, assume $T = 800^\circ\text{C}$, $P = 1 \text{ atm}$, $y_{\text{H}_2\text{O}} = 0.95$, $y_{\text{H}_2} = 0.05$, $y_{\text{O}_2} = 0.05$, $ASR = 0.5 \text{ Ohm cm}^2$, and $\eta_{th} = 0.45$. Under these conditions, the Nernst potential is 0.772 V. If we wish to achieve a current density of 0.25 A/cm^2 , the required operating voltage would be 0.897 V, yielding a hydrogen production efficiency of 0.54 for the assumed power-production efficiency of 0.45. So, with favorable operating conditions, high-temperature electrolysis can yield overall hydrogen-production efficiencies that are higher than the power-cycle thermal efficiency. Furthermore, if the electrolysis process is powered by a high-efficiency advanced reactor/power cycle, overall thermal-to-hydrogen efficiencies greater than 50% can be achieved.

Conventional low-temperature electrolysis would correspond to a power-cycle efficiency around 35% and, due to lower open-cell potentials and higher overpotentials, a per-cell operating voltage in the 1.6 – 1.7 range, yielding overall thermal-to-hydrogen-production efficiencies of less than 35%.

CONCLUSIONS

Thermodynamic performance limits for thermal water splitting processes have been presented. Thermochemical and electrolytic processes can both be included in this category if the electrical power required for electrolysis is based on some

kind of heat engine, such as a gas turbine coupled to a high-temperature reactor. General performance predictions based on simple thermodynamic analyses are consistent with results obtained with detailed system analyses. The unique thermal characteristics of high-temperature electrolysis processes were discussed, including the significance of the thermal neutral voltage and its relationship to the endothermic reaction heat requirement, the electrolysis efficiency, and the isothermal net heat requirement. The effect of area-specific resistance (ASR) and operating voltage on electrolyzer efficiency was discussed. Low ASR values allow for low operating voltages and correspondingly high efficiencies, while still achieving reasonable current densities. Analysis of non-isothermal operation is outlined, along with results of parametric studies. Consideration of overall hydrogen production efficiencies for cases with different heat addition temperatures for the power cycle and the electrolyzer shows that the potential gains to be realized from high-temperature electrolysis are modest, if the power-cycle heat addition temperature (and thermal efficiency) is fixed.

ACKNOWLEDGMENTS

This work was supported by the Idaho National Laboratory, Laboratory Directed Research and Development program and by the U.S. Department of Energy, Office of Nuclear Energy, Nuclear Hydrogen Initiative Program.

COPYRIGHT STATEMENT

This manuscript has been authored by Battelle Energy Alliance, LLC under Contract No. DE-AC07-05ID14517 with the U.S. Department of Energy. The United States Government retains and the publisher, by accepting the article for publication, acknowledges that the United States Government retains a nonexclusive, paid-up, irrevocable, world-wide license to publish or reproduce the published form of this manuscript, or allow others to do so, for United States Government purposes.

REFERENCES

1. Lewis, D., "Hydrogen and its relationship with nuclear energy," *Progress in Nuclear Energy*, Vol. 50, pp. 394-401, 2008.
2. Forsberg, C. W., "Nuclear Hydrogen Production for Liquid Hydrocarbon Transport Fuels," *Proceedings, AIChE Annual Mtg.*, pp. 7988-7995, 2005.
3. Hori, M., "Nuclear Energy for Transportation: Paths through Electricity, Hydrogen, and Liquid Fuels," *Progress in Nuclear Energy*, Vol. 50, pp. 411-416, 2008.
4. Scott, D. S., Smelling Land, *The Hydrogen Defense against Climate Catastrophe*, Canadian Hydrogen Association, 2007.
5. Brown, L. C., Lentsch, R. D., Besenbruch, G. E., Schultz, K. R., "Alternative Flowsheets for the Sulfur-Iodine Thermochemical Hydrogen Cycle," *AIChE Journal*, April 2003.

6. Brown, L. C., Besenbruch, G. E., Lentsch, R. D., Schultz, K. R., Funk, J. F., Pickard, P. S., Marshall, A. C., Showalter S. K., "High Efficiency Generation of Hydrogen Fuels Using Nuclear Power – Final Technical Report for the Period August 1, 1999 through September 30, 2002", Prepared under the Nuclear Energy Research Initiative (NERI) Program Grant No. DE-FG03-99SF21888 for the U.S. Department of Energy, June 2003.
7. Maskalick, N. J., "High Temperature Electrolysis Cell Performance Characterization," *Int. J. Hydrogen Energy*, pp. 563-570, 1986.
8. O'Brien, J. E., Stoots, C. M., Herring, J. S., Lessing, P. A., Hartvigsen, J. J., and Elangovan, S., "Performance Measurements of Solid-Oxide Electrolysis Cells for Hydrogen Production from Nuclear Energy," *Journal of Fuel Cell Science and Technology*, Vol. 2, pp. 156-163, August 2005.
9. O'Brien, J. E., Stoots, C. M., Herring, J. S., and Hartvigsen, J. J., "Hydrogen Production Performance of a 10-Cell Planar Solid-Oxide Electrolysis Stack," *Journal of Fuel Cell Science and Technology*, 3, pp. 213-219, (2006).
10. Yildiz, B., and Kazimi, M. S., "Nuclear Energy Options for Hydrogen and Hydrogen-Based Liquid Fuels Production," MIT-NES-TR-001, September 2003.
11. O'Brien, J. E., McKellar, M. G., and Herring, J. S., "Performance Predictions for Commercial-Scale High-Temperature Electrolysis Plants Coupled to Three Advanced Reactor Types," ANS International Congress on Advances in Nuclear Power Plants (ICAPP08), June 8-12, 2008, Anaheim, CA.
12. Nomura, M., Kasahara, S., and Onuki, K., "Estimation of Thermal Efficiency to produce Hydrogen from Water through IS Process," Proc., 2nd Topical Conference on Fuel Cell Technology, AIChE Spring National Meeting, New Orleans, 2003.
13. Abraham, B. M., and Schreiner, F., "General Principles Underlying Chemical Cycles which Thermally Decompose Water into the Elements," *Ind. Eng. Chem. Fundam.*, Vol. 13, No. 4, 1974.
14. Fletcher, E. A., and Moen, R. L., "Hydrogen and Oxygen from Water," *Science*, Vol. 197, pp. 1050-1056, 1977.
15. UniSim Design, R360 Build 12073, Copyright ©2005-2006 Honeywell International Inc.
16. Brown, L. C., Lentsch, R. D., Besenbruch, G. E., Schultz, K. R., "Alternative Flowsheets for the Sulfur-Iodine Thermochemical Hydrogen Cycle," *AIChE Journal*, April 2003.
17. Yildiz, B., and Kazimi, M. S., "Nuclear Energy Options for Hydrogen and Hydrogen-Based Liquid Fuels Production," MIT-NES-TR-001, September 2003.
18. Southworth, F. H., Macdonald, P. E., Harrell, D. J., Park, C. V., Shaber, E. L., Holbrook, M. R., and Petti, D. A., "The Next Generation Nuclear Plant (NGNP) Project," Proceedings, Global 2003, pp. 276-287, 2003.
19. Singhal, S. C., and Kendall, K., *Solid Oxide Fuel Cells*, Elsevier Advanced Technology, Oxford, UK, 2003.
20. Larminie, J. and Dicks, A., *Fuel Cell Systems Explained*, John Wiley & Sons, New York, 2003.
21. Stoots, C. M., O'Brien, J. E., McKellar, M. G., Hawkes, G. L., and Herring, J. S., "Engineering Process Model for High-Temperature Steam Electrolysis System Performance Evaluation," AIChE 2005 Annual Meeting, Cincinnati, Oct. 30 – Nov. 4, 2005.
22. O'Brien, J. E., Stoots, C. M., and Hawkes, G. L., "Comparison of a One-Dimensional Model of a High-Temperature Solid-Oxide Electrolysis Stack with CFD and Experimental Results," Proceedings, 2005 ASME International Mechanical Engineering Congress and Exposition, Nov. 5 – 11, Orlando.